N. Vasileiadis
D. J. L. Brett
Department of Chemical Engineering,
Imperial College,
London SW7 2AZ, UK

V. Vesovic
Department of Earth Science and Engineering,
Imperial College,
London SW7 2AZ, UK

A. R. Kucernak
Dept. of Chemistry,
Imperial College,
London SW7 2AZ, UK

E. Fontes
Comsol AB,
Stockholm, Sweden

N. P. Brandon[1]
Department of Chemical Engineering,
Imperial College,
London SW7 2AZ, UK
e-mail: n.brandon@imperial.ac.uk

Numerical Modeling of a Single Channel Polymer Electrolyte Fuel Cell

A two-dimensional model of a single-channel polymer fuel cell has been developed. To achieve model validation, current mapping experiments were performed on the cathode side of a single-channel polymer electrolyte fuel cell (PEFC) of various channel widths, at different reactant flow rates and over a range of operating cell voltages. The fuel side was operated in cross-flow mode, with a high stoichiometric excess of hydrogen to ensure no limitations in anode performance as a function of position along the channel. The solution domain comprises seven regions, (two inlet channels, two diffusers, two active catalyst layers, and a membrane) and considers transport of hydrogen and water vapor in the anode and oxygen and nitrogen and water vapor in the cathode. The resulting set of coupled differential equations was solved numerically with FEMLAB®*, a* MATLAB®*-based software. The model has been compared to data from a single-channel PEFC, and good agreement between experiment and theory was obtained.* [DOI: 10.1115/1.2756557]

Introduction

Many polymer electrolyte fuel cell (PEFC) developers have highlighted the measurement and modeling of inhomogeneity in polymer electrolyte fuel cells as one of critical importance to the understanding and development of fuel cell devices. In this context, inhomogeneity is taken to embody such aspects as spatial variation in current density, membrane humidity, reactant concentration, temperature, etc. The approach taken here has been to seek to gain an understanding into these spatial issues by developing a predictive model in two dimensions. To achieve this, we have developed a model of a single-channel PEFC and validated this against experimental data using a previously reported current-mapping technique [1–3]. Use of a single-channel PEFC as opposed to a full flow field represents the simplest possible geometry and one where we have developed techniques that allow model validation. This is the key first step in developing models of more complex and experimentally and numerically validated flow fields.

The first model of a single-channel PEFC based on fundamental equations that incorporated all the regions of the cell was presented by Springer and Raistrick [4]. This was a one-dimensional steady-state model that considered five different regions of unit cross-sectional area within the fuel cell: two inlet channels, two gas-diffusion electrodes, and the Nafion® membrane. External gas humidifiers set the water flow into the inlet channels, and the water flow inside the cell was dependent on the water produced. The authors argued that the convective transport for water is limited to the drag force on water due to proton flux, and therefore, pressure-induced transport was not incorporated. Water transport through the electrodes was taken to occur only as vapor, and no liquid water flux was considered.

In the extension of this work, Springer et al. [5] omitted the anode electrode losses and focused only on the cathode side. This approach is appropriate for the case of a well-humidified cell with a pure H_2 feed stream. The cathode model considered losses caused by the rate of the oxygen reduction reaction, limited ionic conductivity, limited permeability through the hydrophobic backing layer, and the drop in oxygen concentration along the inlet channel caused by reactant consumption. An improved model, looking in detail at the gas transport and ionic conductivity limitations in the catalyst layers and diffusers, was presented in 1993 [6]. This model predicted mass transport limitations at high current densities but used fitted parameters [7] to achieve a good agreement with experimental data. Weisbrot et al. [8,9] extended the work of Springer and Raistrick [4] and Springer et al. [5,6] to predict performance as a function of water balance in the channel and transport across the membrane, though the catalyst layers continued to be treated as finite interfaces.

Springer et al. [10], Zawodzinski et al. [11], and Ren et al. [12] combined experiment with dynamic modeling, to quantify the performance impact of poor water management. To do this, they calculated the impact of water management on both ionic conductivity and the cathodic reaction rate. An important element in their approach was the use of a large experimental database, which they used to fit the model results. The initial work done by Springer and Raistrick [4] and Springer et al. [5], coupled with work by Newman [13], formed the basis of the Bernardi–Verbrugge model [14,15]. Bernardi and Verbrugge proposed a predictive one-

[1]Corresponding author

Submitted to ASME for publication in the JOURNAL OF FUEL CELL SCIENCE AND TECHNOLOGY. Manuscript received November 10, 2005; final manuscript received June 21, 2006. Review conducted by Abel Hernandez.

dimensional steady-state model based on the Nernst–Planck equation, Schögl's velocity equation, the Butler–Volmer equation, and Darcy's law for transport through porous media. These equations, along with appropriate conservation equations, and boundary conditions over the different regions of the cell, formulate a system of differential equations to model the fuel cell. For a solution to be feasible, certain assumptions had to be made. The gases were assumed to be ideal and well mixed. In the gas diffuser regions, the gas pressure was taken to be constant and equal to that of the inlet channels, whereas in the regions of the cell that are not rendered hydrophobic with PTFE (aqueous regions), a hydraulic pressure variation is presumed to exist. The set of equations were further simplified by assuming the catalyst layers to be of vanishing thickness, which is appropriate for operation at high current densities. A second series of assumptions was to take the water-vapor flux in the cathode diffuser to be constant by taking the nitrogen gas mole fraction to be invariant. These simplifications allowed an analytical solution to be constructed for the water velocity and pressure equations in the different parts of the cell, further simplifying the potential and current equations.

In the present work, the approach has been to extend the model developed by Bernardi and Verbrugge [14,15] to two dimensions, also adding extra regions to incorporate the fuel and air channels. However, to extend the model into two dimensions, it was not possible to use simplifying analytical solutions for water velocity and pressure. Instead, the differential equations governing water velocity and pressure were solved numerically. Furthermore, we have also introduced the porous agglomerate concept to describe the behavior of the flooded catalyst regions. The resultant set of equations, constituting the two-dimensional numerical model developed in this study, are presented in the following section.

Model Development

The schematic of the model fuel cell is illustrated in Fig. 1(*a*). There are seven distinctive regions: the two inlet channels, the two gas diffusers, the two catalyst layers, and the membrane. There is an imposed gas flow within the channels in the positive y direction, and the origin of the $y-z$ coordinate system is set at the wall of the anode channel inlet. In the anode, the transport of hydrogen and water vapor is considered and, in the cathode, transport of oxygen, nitrogen, and water vapor is considered. The gases are assumed to be ideal and well mixed, and the cell is considered isothermal. For the transport of reactants, it is assumed that there are pores that are flooded and there are also pores that are rendered hydrophobic, through the use of PTFE, to allow for the transport of gases. The membrane is considered fully and uniformly hydrated. Finally, it is assumed that no transport of hydrogen and oxygen occurs through the membrane, only protons and associated water.

Fuel Cell Chemistry. The electrochemical reactions are confined to the two thin catalyst layer regions. On the anode side, the overall hydrogen reaction can be written as

$$2H_2 \rightarrow 4H^+ + 4e^- \tag{1}$$

indicating that the stoichiometric coefficient for hydrogen is, $s_{H_2} = -2$, while the overall number of electrons exchanged is $n=4$. On the cathode side, the overall oxygen reaction can be written as

$$O_2 + 4H^+ + 4e^- \rightarrow 2H_2O \tag{2}$$

indicating that the stoichiometric coefficient for oxygen and water are $s_{O_2} = -1$ and $s_w = 2$, respectively.

Potential Equations. Because there are two conducting species, namely, electrons and protons, it is necessary to have two potential equations, one for the electronic (referred to with subscript s for solid [4,14]) phase and one for the ionic (referred to with subscript l for liquid [4,14]) phase. The equation for the

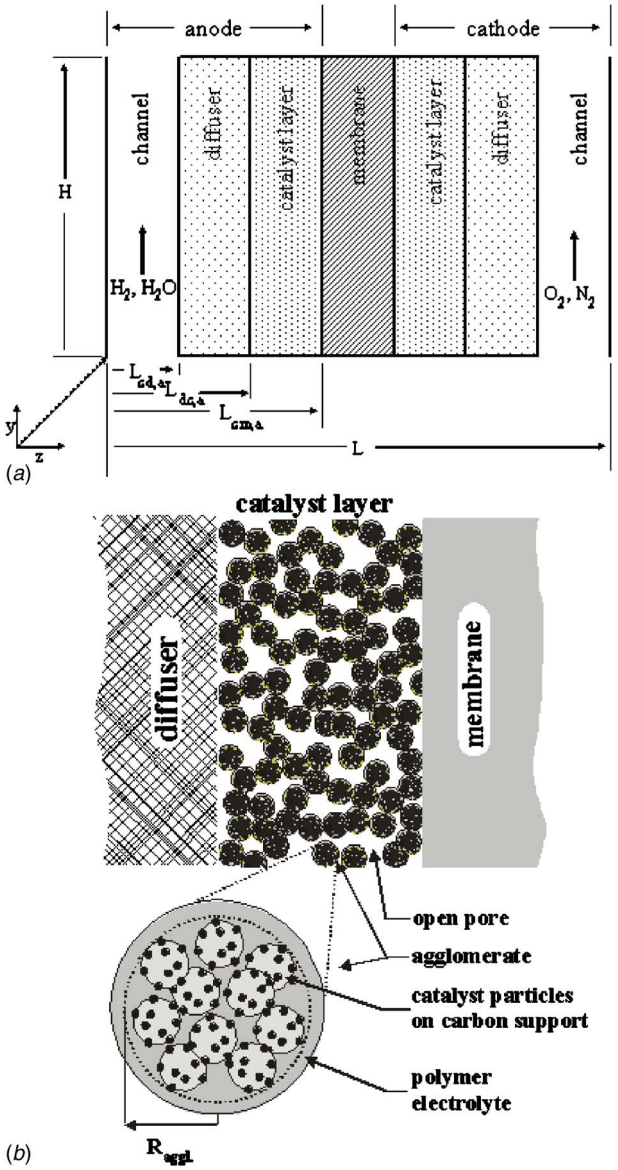

Fig. 1 (*a*) **Schematic of the fuel cell and** (*b*) **schematic of agglomerate model**

electronic potential Φ_s is applicable in the diffusers and the catalyst layers, and that for the ionic potential Φ_l is applicable in the catalyst layers and the membrane.

We assume that the diffusers are good conductors and that the current due to electron transfer will be constant everywhere throughout the diffusers. Hence, the electronic potential in the diffusers is governed by the Laplace equation,

$$\frac{\partial^2 \Phi_s}{\partial z^2} + \frac{\partial^2 \Phi_s}{\partial y^2} = 0 \tag{3}$$

In the catalyst layer, the electronic potential is governed by the Poisson equation, which for the anode catalyst layer is given by

$$-\sigma^{\text{eff}}\left(\frac{\partial^2 \Phi_s}{\partial z^2} + \frac{\partial^2 \Phi_s}{\partial y^2}\right) = -\left(\frac{\partial i_{\text{elect,an}}}{\partial z} + \frac{\partial i_{\text{elect,an}}}{\partial y}\right) \tag{4}$$

The effective electronic conductivity σ^{eff}, where $\sigma^{\text{eff}} = \sigma(1-\varepsilon)$, is used to show that the conductivity in this region is different from that in the diffuser. The porosity of both the anode and

cathode catalyst layers is taken to be constant, so that σ^{eff} is the same in both regions. The same equation can be written for the cathode catalyst layer, but in this case, the electronic anode current density $i_{\text{elect,an}}$ is replaced with the electronic cathode current density $i_{\text{elect,cat}}$. In the rest of the paper, only the equations for the anode side will be given on the understanding that the equivalent equations for the cathode side can be obtained by the exchange of subscript "an" with "cat".

The minus sign in the electronic phase potential of the anode is used because the electronic current decreases at the same rate the ionic current increases. In the case of the cathode catalyst layers, the signs of the current are reversed to reflect the increase of the electronic current as the ionic current decreases.

The ionic current in the anode catalyst layer is also governed by the Poisson equation

$$-k^{\text{eff}}\left(\frac{\partial^2\Phi_l}{\partial z^2}+\frac{\partial^2\Phi_l}{\partial y^2}\right)=\left(\frac{\partial i_{\text{ion,an}}}{\partial z}+\frac{\partial i_{\text{ion,an}}}{\partial y}\right)=-\left(\frac{\partial i_{elect,an}}{\partial z}+\frac{\partial i_{\text{elect,an}}}{\partial y}\right) \tag{5}$$

where the conducting properties of the catalyst layer are now described by the effective ionic conductivity k^{eff}, where $k^{\text{eff}}=k(1-\varepsilon)$. The analogous equation for the ionic potential in the membrane is

$$\frac{\partial^2\Phi_l}{\partial z^2}+\frac{\partial^2\Phi_l}{\partial y^2}=0 \tag{6}$$

In order to calculate the current density, we model both catalyst layers by means of the agglomerate model [16–19]. We assume that the catalyst layers are porous and consist of spherical catalyst agglomerates of average radius R_{aggl}, as illustrated schematically in Fig. 1(*b*). We further assume that agglomerates are themselves porous, but that the size of the pores is much smaller than the size of the voids between agglomerates. We make a further simplification in that we assume that the agglomerates are flooded, while the voids between the agglomerates are sufficiently large that only gas is present. The porosity of the catalyst layer is sufficiently large that, as a first approximation, we can treat the agglomerates as independent of each other. The gaseous reactant (H_2 on the anode side and O_2 on the cathode side) diffuses through the surface of the agglomerate and undergoes an electrochemical reaction inside the agglomerate on the catalytic surface. We assume that all of the reactant that enters the agglomerate undergoes an electrochemical reaction, and hence, the overall current density produced is given by

$$i=(i_{\text{elect}}+i_{\text{ion}})=4n_{\text{aggl}}W_iFd \tag{7}$$

where n_{aggl} is the number of the agglomerates per unit volume of the catalyst layer, F is the Faraday constant, d is the unit depth to alow for scaling of the current density to 2D, and W_i is the mean molar flow of the reactants entering the agglomerate. W_i can easily be related to the molar flux of the reactants at the surface of the agglomerate N_i (e.g., $W_i=4\pi R_{\text{aggl}}^2N_i$), while the number of agglomerates per unit volume n_{aggl} can be related to the porosity of the catalyst layers [18] ε,

$$(1-\varepsilon)=n_{\text{aggl}}\frac{4\pi R_{\text{aggl}}^3}{3} \tag{8}$$

Assuming first-order heterogeneous, electrochemical reactions within the agglomerates at both anode and cathode, the mass conservation equation for species i, inside the agglomerate, reads [18–20],

$$D_i\frac{1}{r^2}\frac{d}{dr}\left(r^2\frac{dc_i}{dr}\right)=k_iS_{\text{aggl}}c_i \quad 0\le r\le R_{\text{aggl}} \tag{9}$$

where c_i and D_i are the concentration and the effective diffusion coefficient of the reacting species, respectively. The quantity k_i is the rate constant of the heterogeneous electrochemical reaction taking place on the active catalyst sites within the agglomerate, and S_{aggl} is the available, active catalytic surface area per unit volume of the agglomerate. By solving Eq. (9), with the appropriate boundary conditions [20], one can obtain the expression for the molar flow W_i as [20]

$$W_i=4\pi R_{\text{aggl}}D_ic_i^{\text{aggl}}\left[1-\sqrt{\frac{k_iS_{\text{aggl}}}{D_i}}R_{\text{aggl}}\coth\left(\sqrt{\frac{k_iS_{\text{aggl}}}{D_i}}R_{\text{aggl}}\right)\right] \tag{10}$$

The concentration of the reactant on the inside surface of the flooded agglomerate c_i^{aggl} can be calculated from the concentration of the reactant in the surrounding gaseous phase through Henry's law,

$$c_i^{\text{aggl}}=\frac{x_iP}{H_i} \tag{11}$$

where P is the pressure inside the catalyst layer, while x_i and H_i are the mole fraction and the Henry' s coefficient for the reacting species, respectively.

The kinetic constant k_i for an electrochemical reaction can be related to the overpotential [13]. For example for the anode,

$$k_i=\frac{j_0}{4Fc^{\text{ref}}}\exp\left(\frac{(1-\alpha_{\text{an}})F}{R\,.\,T}\cdot(\Phi_s-\Phi_m-\Delta\Phi_{\text{an}})\right) \tag{12}$$

where c^{ref} is a standard reference concentration, usually the inlet concentration, j_0 is the exchange current density for the anode α_{an} is the anodic transfer coefficient, Φ_m is the membrane phase potential and $\Delta\Phi_{\text{an}}$ is a reference potential, which we have taken to be the reversible potential of the anode vs. a standard hydrogen electrode.

By substituting Eqs. (8) and (10)–(12) into Eq. (7), we can express the total anode current density as [18]

$$i_{\text{an}}=12(1-\varepsilon)\frac{F\,.\,P}{R_{\text{aggl}}^2}\frac{x_{H_2}D_{H_2}}{H_{H_2}}\left[1-\sqrt{\frac{\frac{j_0}{4Fc^{\text{ref}}}\exp\left(\frac{(1-\alpha_{\text{an}})F}{RT}(\Phi_s-\Phi_m-\Delta\Phi_{\text{an}})\right)S_{\text{aggl}}}{D_{H_2}}}\times R_{\text{aggl}}\coth\left(\sqrt{\frac{\frac{j_0}{4Fc^{\text{ref}}}\exp\left(\frac{(1-\alpha_{\text{an}})F}{RT}(\Phi_s-\Phi_m-\Delta\Phi_{\text{an}})\right)S_{\text{aggl}}}{D_{H_2}}}R_{\text{aggl}}\right)\right] \tag{13}$$

A similar expression can be written for the cathode by replacing subscripts H_2 and "an" with O_2 and "cat", respectively. As the concentration of the gaseous reactants and the overall pressure varies as a function of the position in the catalyst layer, so will the generated current density.

Transport Equations. In order to solve the potential-current equations (Eqs. (3)–(6) and (13)), one needs to evaluate the concentration of species in the channels, diffusers, and catalyst layers. In all three regions, the mass conservation of each species can be expressed in terms of the general diffusion-advection equation

$$-D_i^{\text{eff}}\left(\frac{\partial^2 c_i}{\partial z^2}+\frac{\partial^2 c_i}{\partial y^2}\right)+\frac{\partial(c_i u_z)}{\partial z}+\frac{\partial(c_i u_y)}{\partial y}=R_i \tag{14}$$

where the anode side deals with the concentration change of molecular hydrogen, whereas the cathode side addresses the concentration change of molecular oxygen. The u_y and u_z components of the flow velocity refer to the direction along and perpendicular to the flow, respectively, while R_i is the reaction rate per unit volume for reactions given by Eqs. (1) and (2).

In the channels, no reaction takes place; thus, the term on the right-hand side of Eq. (14) can be set to zero. In practical fuel cells, the flow rates are sufficiently small that the velocity profiles can be obtained from the solutions of Stokes' equations,

$$\frac{\partial P}{\partial z}=\mu\left(\frac{\partial^2 u_z}{\partial z^2}\right);\quad \frac{\partial P}{\partial y}=\mu\left(\frac{\partial^2 u_y}{\partial y^2}\right) \tag{15}$$

where P is the pressure in the channel and μ is the viscosity of the gas flowing through the channel. Perfect gas behavior is assumed, as is the concentrations being proportional to the mole fraction of the species present (e.g., $c_i=x_iP/RT$).

In the diffusers, it is necessary to account for the porosity of the media, which greatly reduces the transport by advection. Hence, Darcy's law is used to approximate the velocity field inside the diffusers

$$u_z=\frac{k_P}{\mu}\frac{\partial P}{\partial z};\quad u_y=\frac{k_P}{\mu}\frac{\partial P}{\partial y} \tag{16}$$

where k_P is the hydraulic permeability of the diffuser material with respect to hydrophobic pores. No reactions take place; thus, R_i is again set to zero.

Inside the catalyst layers, the velocity field is also estimated by means of Darcy's law, (Eqs. (16)), the only difference being the permeability of the domain. Because of the membrane penetration in this region, it is essential to introduce effective permeabilities [15], which are dependent on the extent of the membrane penetration [14,15]. As previously indicated, the effective parameters are simply calculated by multiplying relevant variables by the porosity (for instance, $k_P^{\text{eff}}=\varepsilon_{\text{memb}}k_P$, where $\varepsilon_{\text{memb}}$ is the volume fraction of membrane in the catalyst layer). In the catalyst layer, a reaction term is important since in this region, as well as the transport of species, electrochemical reactions occur. Hence, there is a sink term for the molecular oxygen and hydrogen, and a production term for the ionic current. Therefore, a decrease in the electronic current is observed, as charge transfer from the electronic to the ionic phase occurs in this region. Furthermore, it is assumed there are two modes of transport available, one for gases through pores rendered hydrophobic with PTFE and the other for liquid water through flooded pores. The transport of water is discussed subsequently.

The reaction rate of species i, R_i, is dependent on the current, and for the anode catalyst layer, it is given by

$$R_i=-\frac{1}{4F}\left(\frac{\partial i_{\text{elect,an}}}{\partial z}+\frac{\partial i_{\text{electr,an}}}{\partial y}\right) \tag{17}$$

where the current density is given by Eq. (13).

Water Balance. The water balance included in the present model is based on that presented by Bernardi and Verbrugge [14,15] but generalized to two dimensions. The water balance equations apply in the diffuser, catalyst, and membrane regions. It is assumed that the water velocity in the diffusers can be approximated by the Darcy flow equations together with the continuity equation,

$$v_z=\frac{k_{Pw}}{\mu_w}\frac{\partial P_w}{\partial z};\quad v_y=\frac{k_{Pw}}{\mu_w}\frac{\partial P_w}{\partial y};\quad \frac{\partial v_y}{\partial y}+\frac{\partial v_z}{\partial z}=0 \tag{18}$$

where P_w is the hydraulic pressure, v_z and v_y are the z and y components of the liquid water velocity, respectively, k_{Pw} is the diffuser hydraulic permeability with respect to hydrophilic pores and is taken to be uniform in this region, and μ_w is the viscosity of water.

In the catalyst layers, the velocity is given by Schögl's equations ([14,21], and references therein)

$$v_z=\frac{k_{\Phi w}^{\text{eff}}}{\mu_w}z_f c_f F\frac{\partial \Phi_m}{\partial z}-\frac{k_{Pw}^{\text{eff}}}{\mu_w}\frac{\partial P_w}{\partial z} \tag{19}$$

$$v_y=\frac{k_{\Phi w}^{\text{eff}}}{\mu_w}z_f c_f F\frac{\partial \Phi_m}{\partial y}-\frac{k_{Pw}^{\text{eff}}}{\mu_w}\frac{\partial P_w}{\partial y} \tag{20}$$

where Φ_m is the potential drop across the membrane, and z_f and c_f are the charge and the concentration of the fixed charges in the membrane, respectively. The parameters $k_{\Phi w}^{\text{eff}}$ and k_{Pw}^{eff} are the effective electrokinetic and hydraulic permeabilities, respectively, and are dependent on the extent the membrane penetrates the catalyst layer. The first term on the right-hand side of the Eqs. (19) and (20) gives velocity due to the electromigration of charged species, whereas the second is the advection term. In the cathode catalyst layer, the continuity equation needs to be adjusted to allow for the production of water,

$$\left(\frac{\partial v_z}{\partial z}+\frac{\partial v_y}{\partial y}\right)=-\frac{1}{2F\rho_w}\left(\frac{\partial i_{\text{elect,cat}}}{\partial z}+\frac{\partial i_{\text{elect,cat}}}{\partial y}\right) \tag{21}$$

where ρ_w is the density of water.

Finally, in the membrane, the equations for the water velocity are also given by Eqs. (19) and (20), but with membrane electrokinetic and hydraulic permeabilities k_{Φ}^{mem} and k_P^{mem} replacing the effective ones, $k_{\Phi w}^{\text{eff}}$ and k_{Pw}^{eff}.

Boundary Conditions. On the channel inlet boundary, the mole fraction of hydrogen (anode) and oxygen (cathode), together with the inlet pressure are specified

$$x_i\big|_{y=0}=x_{i,\text{inlet}};\quad P\big|_{y=0}=P_{\text{inlet}} \tag{22}$$

On the channel exit boundary, it is assumed that the transport is only by advection along the direction of flow and the boundary conditions are specified in terms of the flux normal to the boundary,

$$\left.\frac{\partial(c_i u_y)}{\partial y}\right|_{y=H}=N_i\big|_{y=\text{H}};\quad P\big|_{y=\text{H}}=P_{\text{atm}} \tag{23}$$

The above conditions reflect the fact that unreacted gases leave the cell through the outlet at atmospheric pressure.

At the anode channel/diffuser interface, the electronic potential is set to zero (see Fig. 1 for notation),

$$\Phi_s\big|_{z=L_{cd,a}}=0 \tag{24}$$

and at the cathode channel/diffuser interface the electronic potential is set equal to the cell voltage,

$$\Phi_s\big|_{z=L_{cd,c}}=V_{\text{cell}} \tag{25}$$

The pressure and concentrations of all species are set to be continuous at this boundary. For continuity purposes, it is assumed that at the channel/diffuser interface the component of the velocity in the direction of the flow is nonzero. It is taken as the velocity on the diffuser side of the interface. Hence, the velocity boundary conditions at this interface are given by

$$u_y|_{z=L_{cd}} = -\frac{k_p}{\mu}\frac{\partial P}{\partial y}\bigg|_{z=L_{cd}}; \quad u_z|_{z=L_{cd}} = -\frac{k_p}{\mu}\frac{\partial P}{\partial z}\bigg|_{z=L_{cd}} \tag{26}$$

At the diffuser/catalyst layer interfaces, the composition, pressure, velocity, and the electronic potential are assumed to be continuous. The ionic potential at this interface is calculated based on the cell voltage, the conductivity, and the exchange current densities. As the membrane is impermeable to the transfer of uncharged species, the concentration of uncharged species at the catalyst layer/membrane interface are specified in terms of von Neumann boundary conditions,

$$\frac{\partial c_i}{\partial z}\bigg|_{z=L_{cm}} = 0 \quad i = H_2, O_2, H_2O. \tag{27}$$

The pressure and the ionic potential are taken as continuous across the catalyst layer/membrane interface.

All the outside walls enclosing the fuel cell are assumed impermeable to the flux of material or current, and hence, von Neumann boundary conditions for the concentration and potential are used. At the two outer walls of the channels, the no-slip assumption is made about the fluid velocity and both y and z components are taken as zero.

Method of Solution

Because of the difference in region widths (10 μm wide catalyst layer and 1 mm wide channel), and the difference between the length (0.11 m) and the width, the working equations were scaled to [0,1] in each region, both on the z- and y-axes. The resulting dimensionless equations with the relevant boundary conditions presented in the previous sections had to be solved simultaneously and the set of coupled differential equations was solved numerically using FEMLAB®, a MATLAB®-based software specifically designed for chemical engineering modeling. It uses the variational finite element method (FEM) with triangular meshing, and a choice of basis functions (linear, quadratic, cubic, or quartic) according to the complexity of each problem. For the above simulations, the GMRES iterative solver with incomplete lower and upper (LU) (UMFPACK) as a preconditioner was used [22–24]. The mesh comprised triangular quadratic Lagrangian elements with node points at the corners and also at the midpoints of each side of mesh triangles. For each of these nodes, there is one degree of freedom and one basis function. The physical constants and parameters used in the model are detailed in Table 1.

Table 1 Physical constants and parameters used in the model

Quantity	Value
Membrane thickness	0.00012 m [1]
Anode/cathode diffuser thickness	0.00015 m [1]
Cell length	0.11 m [1]
Anode/cathode catalyst layer thickness	0.00001 m [1]
Anode/cathode channel width	0.0001 m [1]
Reference pressure, P	1.01325×10^5 Pa
Temperature, T	353 K
Ionic conductivity, k	3.37 Ω^{-1} m [27,28]
Charge of fixed (sulfonate) species, z_f	−1 [14]
Fixed charge concentration, c_f	1.2×10^3 mol m^{-3} [14]
Dissolved oxygen diffusivity, D_{O_2}	1.2×10^{-10} m^2 s^{-1} [14]
Dissolved hydrogen diffusivity, D_{H_2}	2.59×10^{-10} m^2 s^{-1} [15]
Electrokinetic permeability, k_Φ	1.13×10^{-19} m^2 [15]
Hydraulic permeability, k_P	1.8×10^{-18} m^2 [15]
Pore-water viscosity, μ_w	8.91×10^{-4} Pa s [4]
Pore- water density, ρ_w	54×10^3 mol m^{-3} [4]
Henry's constant for O_2, H_{O_2}	3.2×10^4 Pa m^3 mol^{-1}
Henry's constant for H_2, H_{H_2}	3.9×10^4 Pa m^3 mol^{-1}
Anodic exchange current density, $j_{0,an}$	1.0×10^5 A m^{-2} [15,29]
Cathodic exchange current density, $j_{0,cat}$	1.0 A m^{-2} [15,29]
Agglomerate radius, R_{aggl}	1.0×10^{-7} m
Available active surface area per unit volume of the catalyst layer, S_{aggl}	1.0×10^7 m^{-1}
Reference concentration of hydrogen, c^{ref}	1200 mol m^{-3} [15,30]
Reference concentration of oxygen, c^{ref}	3.39 mol m^{-3} [15,30]
Electronic conductivity, σ	100 Ω^{-1} m^{-1} [14,31]
Diffuser hydraulic permeability in water pores,[a] k_{Pw}	1.0×10^{-16} m^2
Volume fraction of membrane in the catalyst layer, ε_{memb}	0.5 [14]
Diffuser layer porosity, ε	0.75 [1]
Anodic and cathodic transfer coefficient, α	0.5 [14]

[a]This is an interpolated value from data found in the literature.

Model Results and Validation Against Experimental Data

We have previously reported developments in the current-mapping technique [1–3], and its use in characterizing spatial variations in current density along a single-channel PEFC. In this study, current density distribution measurements made using these techniques on a single-channel flow geometry are used to validate the model reported above.

Experimental Method and Procedure. Although full experimental details have been published previously [1], it is beneficial to give a brief description that will allow differences between the actual measurements and the simulation results to be determined.

Current density measurements are made at the interface with the gas diffusion layer (GDL) using an array of contacts fabricated using the printed circuit board (PCB) approach, similar to that of Cleghorn et al. [25]. The use of a PCB has several important advantages: individual contacts can be designed with precise dimensions and can be in very close proximity to each other (as low as 0.2 mm feature spacing); plated through hole (PTH) features can be used to make the connection from the bottom to the top of the board at any point across the surface; PCB material is easily machined and compatible with the internal environment of the fuel cell; PTH contacts can be used to install a separate sense contact associated with each current collector to compensate for lead, connect, and contact resistance; each contact is gold plated to reduce contact resistance and improve corrosion resistance; and the dimension of each current contact can be reduced to the order of 2 mm.

Each contact is associated with its own load circuit; this is effectively a high current potentiostat. By using the sense contact associated with each current contact, the load circuit can compensate for all electrical losses and accurately set the same potential at the point at which each electrode makes contact with the GDL. The set potential of each contact is generated from a single source and sent to each electronic load. To ensure minimal lateral current flow between adjacent contacts, the deviation in the set potential at the contact with the GDL must be < 100 μV. Since the current measurement is being made on an isopotential surface, segmentation of the membrane electrode assembly (MEA) is not necessary. The electronics used make the system equally applicable to the study of the anode or cathode with minimal reconfiguration required. This system can be tailored to study most types of flow-field features and can be applied to "off-the-shelf" MEAs without any modifications or detriment to the components. Associating each contact with its own electronic load allows real-time data collection to be achieved [1] and, with minimal adaptation, the system can be configured to allow localized impedance measurements [2] and conductivity mapping [26].

To achieve model validation, current mapping experiments were performed on the cathode side of a single-channel PEFC of various channel widths, at different reactant flow rates, and over a range of operating cell voltages. The fuel side was operated in cross-flow mode, with a very high stoichiometric excess of hydrogen used to ensure that there were no limitations in anode perfor-

mance as a function of position along the channel. The operating conditions investigated were chosen to represent significantly different modes of operation of the fuel cell, ranging from high stoichiometry ($\lambda - 20$) to low stoichiometry values ($\lambda - 1.01$). The cell potential ranged from low load (ca.0.7 V) close to the typical operating voltage of a cell, down to high load (ca.0.3 V) representing an inefficient mode of operation in a range characterized by mass transport limitation and high Ohmic losses.

The channel widths investigated were 0.5 mm, 1 mm, and 2 mm, at air flow rates of 50 $cm^3\,min^{-1}$, 30 $cm^3\,min^{-1}$, 20 $cm^3\,min^{-1}$, 10 $cm^3\,min^{-1}$ and 5 $cm^3\,min^{-1}$. Given the large amount of data generated, only a sample of these results will be used for comparison with model prediction.

There are various sources of error associated with the current distribution measurements that should be noted. First, lateral current flow from a region outside the local sampling zone can lead to larger currents being measured at the expense of a lower current measured within the sampling zone from where the lateral current originated. This can lead to a "zigzagging" effect on the current distribution. This is seen, to a certain extent, in the experimental results but does not influence the general trend of the current distribution. Electrical noise can lead to some instability in the current distribution; however, this interference can be brought to an acceptable level using signal averaging. Variations in the physical properties of the MEA caused by changes over time or manufacturing inconsistencies can lead to current density variations that are not a result of the operating conditions of the fuel cell and are not accounted for in the model. We have used the current mapping technique to identify current variations caused by such factors [1]. Membrane dehydration can lead to current variations, which are not as yet accounted for in the model; this is most likely to affect the early portions of the channel when operating at higher reactant flow rates. Using localized conductivity measurements, the state of the membrane hydration has been investigated using this same technique [26].

Values of current are reported as Amperes per centimeters to the −2, with the area to which each local current is scaled corresponds to the area of the channel for that portion of the fuel cell. Since a certain amount of reactant diffusion will occur to catalyst sites laterally away from the channel area, experimental values of current density will appear to be higher than those reported in fuel cells, which have a flow field that covers the entire surface of the MEA. However, as demonstrated by Kornyshev and Kulikovsky [27], when a fuel cell is operating under a moderate load, the reactant distribution and current generated is largely confined to the open area of the fluid flow channel.

Predicted Current, Concentration, and Pressure Profiles. The results are presented in three sections. In the first section, figures illustrating the profiles of system variables are presented for different cell voltages using the constants, conditions, and cell geometry reported in Table 1. In the second section, graphs comparing experimental and model results for different flow rates and inlet channel widths are presented. Finally, localized polarization plots from both model and experiment are compared. It should be noted that, because of the anisotropic scaling, the widths of the different regions, as well as the length of the cell, are reported as unity, with the length being elongated to illustrate the along-the-channel dimension.

Figure 2(*a*) illustrates the ionic current density midway between the channel inlet and outlet (i.e., in the z direction at $y=H/2$) for cell voltages of 0.4 V, 0.6 V, and 0.8 V. As can be seen, due to the fast hydrogen reaction kinetics in the anode catalyst layer, the current rises rapidly in the vicinity of the anode/membrane interface, whereas in the cathode the rise of the ionic current is distributed more evenly across the catalyst layer. Figure 2(*b*) shows the corresponding distribution of electronic current density. In the anode catalyst layer, the majority of the anode reaction occurs close to the membrane, due to the effect of high conductivity in the electronically conducting phase coupled with fast reaction kinetics. Similar behavior is observed in the cathode, but the reaction zone is more evenly distributed due to the slower reaction kinetics.

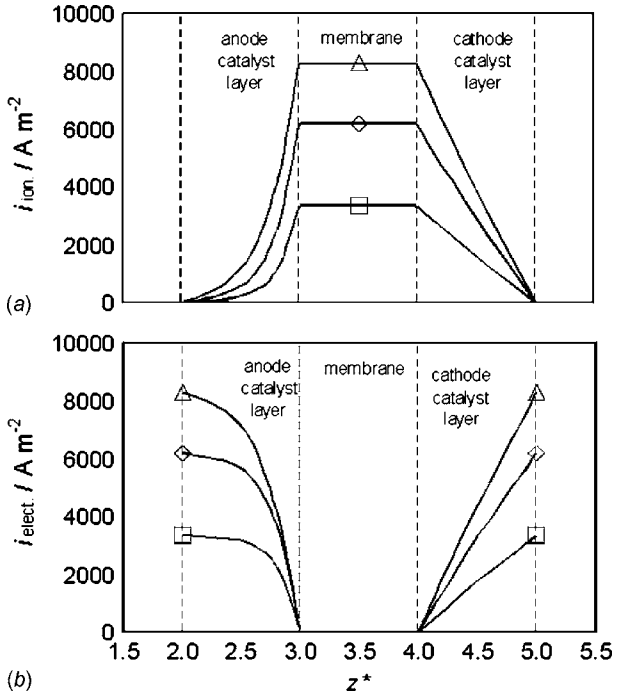

Fig. 2 Predicted current density across the middle of the cell ($y=H/2$) for various cell voltages: –□– 0.8 V, –◇– 0.6 V, –△– 0.4 V, under the conditions detailed in Table 1: (*a*) ionic current density and (*b*) electronic current density

Figure 3 shows the variation in ionic current density along the middle of the membrane (in the y direction) for different cell voltages. As expected, the current density at the channel inlet increases with decreasing cell voltage but decreases with distance along the channel due to reactant depletion. In the case of a 0.4 V cell voltage, the current density is substantially lower close to the outlet as a result of reactant depletion near the inlet. The flow rate in the channel was kept constant and the same in all three cases.

Figure 4 shows the distribution of the ionic potential in the ionically conducting phase across the middle of the cell (i.e., the z direction at $y=H/2$) for different cell voltages. There is a significant potential drop across the membrane, reflecting its relatively

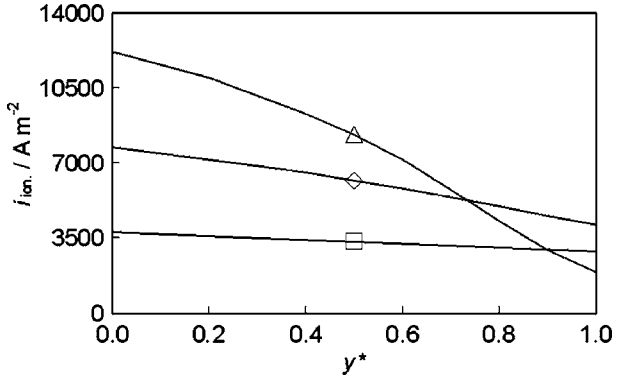

Fig. 3 Predicted ionic current density along the middle of the membrane ($z=L/2$) for different cell voltages: –□– 0.8 V, –◇– 0.6 V, –△– 0.4 V, under the conditions detailed in Table 1

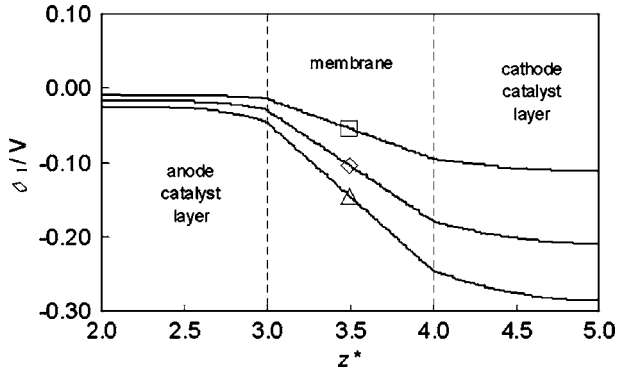

Fig. 4 Predicted ionic potential across the middle of the cell ($y=H/2$) for various cell voltages: –□– 0.8 V, –◇– 0.6 V, –△– 0.4 V, under the conditions detailed in Table 1

low conductivity. This potential gradient drives the transfer of protons from the anode to the cathode and, as expected, increases as the current density increases.

Figure 5 shows the variation in the mole fraction of hydrogen down the anode channel (in the y direction) for different cell voltages. It is assumed that the inlet stream comprises 60% hydrogen and 40% water, being representative of an average fuel composition within a PEFC stack. At high cell voltages and, hence, low current densities, the utilization of the reactants is much smaller than at low cell voltages, for a given reactant flow rate. Figure 5 also shows the mole fraction of oxygen in the inlet channel of the cathode. The cathode feed is assumed to be air comprising 21% oxygen and 79% nitrogen. The flow rate was kept constant and equal to that in the anode.

Figure 6(*a*) shows the pressure profile for different cell voltages. The flow rate in the channel in all three cases is the same. Figure 6(*b*) shows the hydraulic pressure across the middle of the cell for various cell voltages, and it is clear that the higher the current density the higher the hydraulic pressure increase in the cathode.

Model Validation. In this section, three case studies are used to explore the agreement between model and experiment for a range of oxygen utilizations using a variety of channel widths, airflow rates, and cell voltages. The first, illustrated in Fig. 7(*a*), shows the comparison between experimental and model results for a 1 mm channel width using 30 $cm^3\,min^{-1}$ airflow rate at a cell voltage of 0.8 V. The current distribution is almost uniform and varies little with distance along the channel, as the high flow rate combined with the high cell voltage does not lead to significant oxygen depletion, and good agreement between experiment and

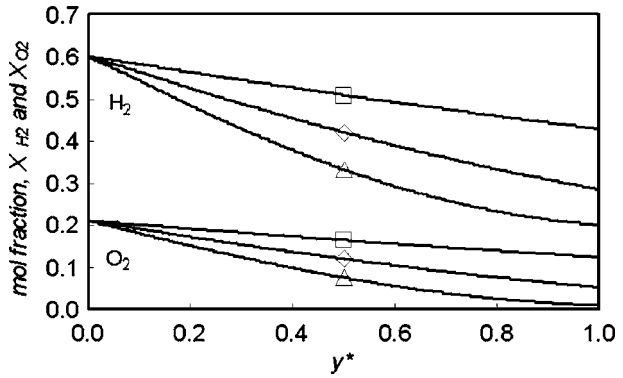

Fig. 5 Predicted hydrogen and oxygen mole fraction down the centre of the channels at different cell voltages: –□– 0.8 V, –◇– 0.6 V, –△– 0.4 V, under the conditions detailed in Table 1

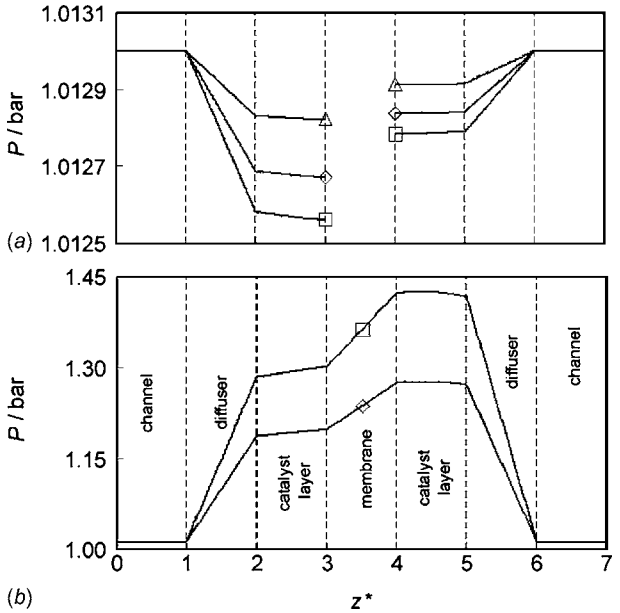

Fig. 6 Predicted pressure profile across the middle of the cell ($y=H/2$) at different cell voltages: –□– 0.8 V, –◇– 0.6 V, –△– 0.4 V, under the conditions detailed in Table 1: (*a*) reactant gas pressure and (*b*) hydraulic liquid water pressure

the model can be observed.

The next case presented in Fig. 7(*b*) is for a 2 mm channel width and 20 $cm^3\,min^{-1}$ airflow rate at a cell voltage of 0.5 V. Here, it can be seen that, because of the lower cell voltage, greater current density, and the wider channel, a larger current is seen at the start of the channel, with a rapid decay to zero toward the exit due to oxygen depletion. A reasonable agreement is obtained between experiment and model, with the disparity between the two at the immediate entry to the channel probably being due to localized membrane dehydration, which is not accounted for in the model.

The final case presented in Fig. 7(*c*) is for 0.5 mm channel width and 10 $cm^3\,min^{-1}$ airflow rate at a cell voltage of 0.3 V. Here, the initial current density at the inlet is high due to the low cell voltage, but soon after, it starts to fall and, after 80% of the channel length, the current falls to near zero as a result of the oxygen depletion. Again, the model gives good agreement with the experimental trends.

Overall, the results show very good agreement between experiment and model, particularly in the cases where reactant concentration falls and the current is small. The strong agreement between model and experiment at high utilization suggest that the model provides a good description of reactant depletion and mass transport effects. However, there is some disparity near the channel inlet, indicating the importance of factors such as membrane hydration, which are not yet accounted for in the model.

Thus far, experimental data have been compared to the model predictions for the length of the channel at discrete potentials. However, use of the current mapping technique also allows the model output to be validated against localized polarization plots, and here we report comparisons at the beginning (0.0065 m; $y^*=0.06$), middle (0.055 m; $y^*=0.5$), and end (0.0975 m; $y^*=0.89$) of the channel. It should be noted that the range of the experimental data lies between 0.8 V and 0.1 V, whereas the calculated data range is between 0.8 V and 0.2 V. Furthermore, experimental data were obtained every 20 mV as opposed to every 100 mV with the model. Figure 8 shows the polarization plots at the beginning, middle, and end of the cell for an airflow rate of 10 $cm^3\,min^{-1}$ and a channel width of 1 mm.

By comparison of these localized responses to the overall po-

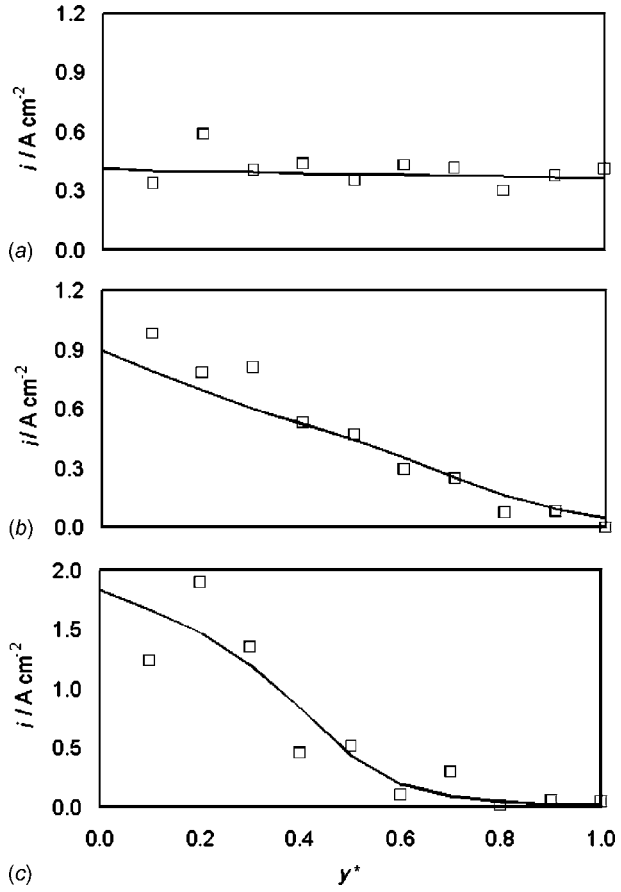

Fig. 7 Comparison between experimental and calculated current density on the cathode side of: (*a*) 1 mm wide single channel PEFC, with a 30 cm^3 min airflow rate at a cell voltage of 0.8 V; (*b*) 2 mm wide single-channel PEFC, with a 20 cm^3 min^{-1} airflow rate at a cell voltage of 0.5 V; (*c*) 0.5 mm wide single-channel PEFC, with a 10 cm^3 min^{-1} flow rate at a cell voltage of 0.3 V

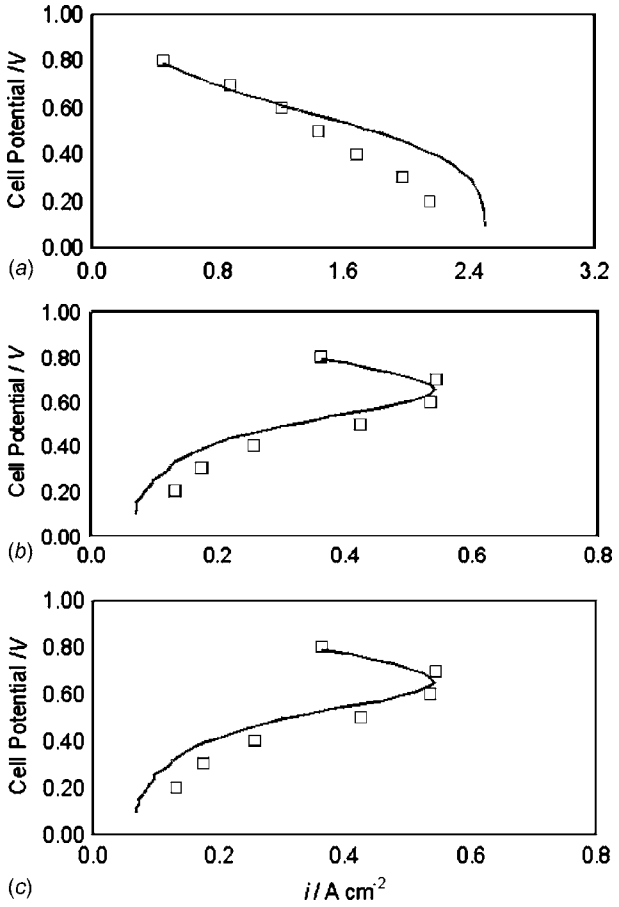

Fig. 8 Predicted and measured cathode polarization plots in the single-channel PEFC for an airflow rate of 10 cm^3 min^{-1} and a channel width of 1 mm: (*a*) at the beginning (0.0065 m) of the channel, (*b*) at the middle (0.05 m) of the channel, and (*c*) at the end (0.0975 m) of the channel

larization plot for the whole single-channel PEFC (which have been previously reported [1]), it is evident that the localized polarization plots are not of the same form as the average bulk response. In particular, the mass transport limiting current can form a maximum and, subsequently, decrease with increasing overpotential. Such a response may, on first inspection, seem counter intuitive; this could be construed to imply that for a given current density, the cell can exist at two different potentials. However, it must be remembered these are localized responses that will be influenced by the upstream consumption of oxygen. Since air entering at the start of the channel will be continuously depleted of oxygen as it traverses the channel, the supply of reactant downstream of a given point will be dynamically affected by the amount of reactant consumed at that point, which in turn is determined by the load on the cell. Therefore, the only part of a fuel cell where the performance is entirely governed by the amount of reactant feed is at the entrance of the cell, before any reactant has been consumed. This mode of behavior has previously also been identified using fuel cell localized electrochemical impedance spectroscopy (FCLEIS) [2].

It can be seen that there is robust agreement between the measured data and that predicted by the model, particularly in Figs. 8(*b*) and 8(*c*), showing the ability of the model to accurately predict mass transfer limitations within the channel. The agreement is less well defined in Fig. 8(*a*), a condition where the reactant utilization is not high, showing that further work is needed to fully describe this region of the fuel cell.

The model prediction of the local polarization response and its agreement with the experimental data is compelling evidence for the validity of the model. To our knowledge, we have been the first to report the existence of the current inversion characteristic in the localized current response under conditions of reactant starvation. The model accurately predicts this feature giving credence to the model and endorsing our interpretation of the feature as being due to reactant starvation.

Conclusions

In this paper, the equations constituting the two-dimensional numerical PEFC model have been presented, as well as model results showing the behavior of system variables under different load conditions. The model allows for parameters relating both to the microstructure and macrostructure of the cell, and is also modular to allow for a variety of case studies and geometries to be examined, giving good insight into fuel cell structure and operation. The model results have been compared to experimental data on a single-channel PEFC obtained using current-mapping techniques, which showed good agreement between modeling and experimental results for a variety of operating conditions and cell geometries tested in this study.

Acknowledgment

We wish to thank Johnson Matthey for providing MEAs, Simon Turner and Steve Atkins for help with fuel cell construction, and

the UK EPSRC for providing funding for D. Brett and N. Vasileiadis under Grant No. GR/M 73552.

Nomenclature

c_i = concentration of species i, mol m^{-3}
c_i^{aggl} = concentration of the reactant inside the agglomerates, mol m^{-3}
c^{ref} = reference concentration, mol m^{-3}
c_f = concentration of the fixed charges in the membrane, mol m^{-3}
D_i = diffusion coefficient of species i, m^2 s^{-1}
D_i^{eff} = effective diffusion coefficient of species i, m^2 s^{-1}
F = Faraday's constant, C mol^{-1}
H_i = Henry's constant, Pa m^3 mol^{-1}
i = total current density, A m^{-2}
i_{elect} = electronic current density, A m^{-2}
i_{ion} = ionic current density, A m^{-2}
j_0 = exchange current density, A m^{-2}
k_i = first-order heterogeneous electrochemical reaction rate constant, m s^{-1}
k^{eff} = effective ionic conductivity, Ω^{-1} m^{-1}
k_{Φ}^{mem} = electrokinetic permeability, m^2
$k_{\Phi w}^{\text{eff}}$ = effective electrokinetic permeability, m^2
k_p = diffuser permeability in hydrophobic pores, m^2
k_{pw} = diffuser hydraulic permeability of water in hydrophilic pores, m^2
k_{pw}^{eff} = effective hydraulic permeability in the hydrophilic pores, m^2
N_i = flux of species i, mol m^{-2} s^{-1}
n_{aggl} = number of agglomerates per unit volume of the catalyst layer, m^{-3}
P = pressure, Pa
P_w = hydraulic water pressure, Pa
R = Gas constant, J mol^{-1} K^{-1}
R_{aggl} = average radius of agglomerates, m
R_i = chemical reaction rate, mol m^{-3} s^{-1}
S_{aggl} = available active surface area unit volume of agglomerates, m^{-1}
T = temperature, K
u = gas velocity, m s^{-1}
v = liquid water velocity, m s^{-1}
V = cell voltage, V
W_i = mean molar flow of species $i$at the surface of agglomerates, mol s^{-1}
x_i = mole fraction of the species in the gas phase
z_f = charge of the fixed charges in the membrane
α = electrochemical kinetics transfer coefficient
ε = catalyst layer porosity
$\varepsilon_{\text{memb}}$ = volume fraction of membrane in the catalyst
$\Delta\Phi_{\text{an}}$ = reference potential, V
Φ_m = membrane potential, V
Φ_s = electronic potential, V
Φ_l = ionic potential, V
μ = gas viscosity, Pa s
μ_w = viscosity of water, Pa s
ρ_w = water density, mol m^{-3}
σ^{eff} = effective electronic conductivity, Ω^{-1} m^{-1}

References

[1] Brett, D. J. L., Atkins, S., Brandon, N. P., Vesovic, V., Vasileiadis, N., and Kucernak, A. R., 2001, "Measurement of the Current Distribution Along a Single Flow Channel of a Solid Polymer Fuel Cell," Electrochem. Commun., **3**(11), pp. 628–632.

[2] Brett, D. J. L., Atkins, S., Brandon, N. P., Vesovic, V., Vasileiadis, N., and Kucernak, A. R., 2003, "Localized Impedance Measurements Along a Single Channel of a Solid Polymer Fuel Cell," Electrochem. Solid-State Lett., **6**(4), pp. A63–A66.

[3] Brett, D. J. L., Atkins, S., Brandon, N. P., Vesovic, V., Vasileiadis, N., and Kucernak, A. R., 2004, "Investigation of Reactant Transport within a Polymer Electrolyte Fuel Cell Using Localised CO Stripping Voltammetry and Adsorption Transients," J. Power Sources, **133**(2), pp. 205–213.

[4] Springer, T. E., and Raistrick, I. D., 1989, "Electrical-Impedance of a Pore Wall for the Flooded-Agglomerate Model of Porous Gas-Diffusion Electrodes," J. Electrochem. Soc., **136**(6), pp. 1594–1603.

[5] Springer, T. E., Zawodzinski, T. A., and Gottesfeld, S., 1991, "Polymer Electrolyte Fuel Cell Model," J. Electrochem. Soc., **138**(8), pp. 2334–2342.

[6] Springer, T. E., Wilson, M. S., and Gottesfeld, S., 1993, "Modelling and Experimental Diagnostics in Polymer Electrolyte Fuel-Cells," J. Electrochem. Soc., **140**(12), pp. 3513–3526.

[7] Eaton, B. M., 2001, "One Dimensional, Transient Model of Heat, Mass, and Charge Transfer in a Proton Exchange Membrane," M.Sc. dissertation thesis, Virginia Polytechnic and State University, Blacksburg, VA.

[8] Weisbrot, K. R., Grot, S. A., and Vanderborgh, N. E., 1995, "Through-the-Electrode Model of a Proton Exchange Membrane Fuel Cell," Proc.-Electrochem. Soc., **95-23**, pp. 152–166.

[9] Weisbrot, K. R., Vanderborgh, N. E., and Grot, S. A., 1996, "Modeling of Gaseous Flows within Proton Exchange Membrane Fuel Cell," *Proc. of Fuel Cell Seminar*, Orlando, Courtesy Associates, Washington, DC, pp. 635–638.

[10] Springer, T. E., Zawodzinski, T. A., Wilson, M. S., and Gottesfeld, S., 1996, "Characterization of Polymer Electrolyte Fuel Cells Using AC Impedance Spectroscopy," J. Electrochem. Soc., **143**(2), pp. 587–599.

[11] Zawodzinski, T. A., Davey, J., Valerio, J., and Gottesfeld, S., 1995, "The Water-Content Dependence of Electroosmotic Drag in Proton-Conducting Polymer Electrolytes," Electrochim. Acta, **40**(3), pp. 297–302.

[12] Ren, X., Springer, T. E., and Gottesfeld, S., 2000, "Water and Methanol Uptakes in Nafion Membranes and Membrane Effects on Direct Methanol Cell Performance," J. Electrochem. Soc., **147**(1), pp. 92–98.

[13] Newman, J. S., 1991, *Electrochemical Systems*, 2nd ed., Prentice-Hall, Englewood Cliffs, NJ.

[14] Bernardi, D. M., and Verbrugge, M. W., 1991, "Mathematical-Model of a Gas-Diffusion Electrode Bonded to a Polymer Electrolyte," AIChE J., **37**(8), pp. 1151–1163.

[15] Bernardi, D. M., and Verbrugge, M. W., 1992, "A Mathematical-Model of the Solid-Polymer-Electrolyte Fuel-Cell," J. Electrochem. Soc., **139**(9), pp. 2477–2491.

[16] Iczkowski, R. P., and Cutlip, M. B., 1980, "Voltage Losses in Fuel-Cell Cathodes," J. Electrochem. Soc., **127**(7), pp. 1433–1440.

[17] Gloaguen, F., and Durand, R., 1997, "Simulations of PEFC Cathodes: An Effectiveness Factor Approach," J. Appl. Electrochem., **27**(9), pp. 1029–1035.

[18] Perry, M. L., Newman, J., and Cairns, E. J., 1998, "Mass Transport in Gas-Diffusion Electrodes: A Diagnostic Tool for Fuel-Cell Cathodes," J. Electrochem. Soc., **145**(1), pp. 5–15.

[19] Jaouen, F., Lindbergh, G., and Sundholm, G., 2002, "Investigation of Mass-Transport Limitations in the Solid Polymer Fuel Cell Cathode—I. Mathematical Model," J. Electrochem. Soc., **149**(4), pp. A437–A447; Jaouen, F., Lindbergh, G., and Sundholm, G., J. Electrochem. Soc., **149**(4), pp. A448–A454.

[20] Bird, B., Stewart, W. E., and Lightfoot, E. N., 2001, *Transport Phenomena*, 2nd ed., Wiley, New York.

[21] Schögl, R., 1966, "Membrane permeation in Systems Far From Equilibrium," Ber. Bunsenges. Phys. Chem., **70**, pp. 400–414.

[22] Deuflhard, P., 1974, "Modified Newton Method for Solution of Ill-Conditioned Systems of Non-Linear Equations With Application to Multiple Shooting," Numer. Math., **22**(4), pp. 289–315.

[23] Deuflhard, P., 1979, "Stepsize Control for Continuation Methods and Its Special Application to Multiple Shooting Techniques," Numer. Math., **33**(2), pp. 115–146.

[24] COMSOLAB, ed., 2001, FEMLAB 3.0 User's Guide, Comsol, Stockholm.

[25] Cleghorn, S. J. C., Derouin, C. R., Wilson, M. S., and Gottesfeld, S., 1998, "A Printed Circuit Board Approach to Measuring Current Distribution in a Fuel Cell," J. Appl. Electrochem., **28**(7), pp. 663–672.

[26] Kulikovsky, A. A., Kucemak, A., and Kornyshev, A. A., 2005, "Feeding PEM Fuel Cells," Electrochim. Acta, **50**(6), pp. 1323–1333.

[27] Kornyshev, A. A., and Kulikovsky, A. A., 2001, "Characteristic Length of Fuel and Oxygen Consumption in Feed Channels of Polymer Electrolyte Fuel Cells," Electrochim. Acta, **46**(28), pp. 4389–4395.

[28] Kulikovsky, A. A., 2001, "Quasi Three-Dimensional Modelling of the PEM Fuel Cell: Comparison of the Catalyst Layers Performance," Fuel Cells, **1**(2), pp. 162–169.

[29] West, A. C., and Fuller, T. F., 1996, "Influence of Rib Spacing in Proton-Exchange Membrane Electrode Assemblies," J. Appl. Electrochem., **26**(6), pp. 557–565.

[30] Simoglou, A., Argyropoulos, P., Martin, E. B., Scott, K., Morris, A. J., and Taama, W. M., 2001, "Dynamic Modelling of the Voltage Response of Direct Methanol Fuel Cells and Stacks Part II: Feasibility Study of Model-Based Scale-Up and Scale-Down," Chem. Eng. Sci., **56**(23), pp. 6773–6779.

[31] Nguyen, T. V., and White, R. E., 1993, "A Water and Heat Management Model for Proton-Exchange-Membrane Fuel-Cells," J. Electrochem. Soc., **140**(8), pp. 2178–2186.